



Surface Reflectance Correction using Constrained Harmonization for Optical Satellite Imagery

Lino Garda Denaro¹ and Chao-Hung Lin¹
¹National Cheng Kung University, Tainan, Taiwan
Email: dgarda.lino@gmail.com

KEY WORDS: Surface reflectance, constrained image harmonization, spectral consistency, temporal consistency.

ABSTRACT: Surface reflectance derived from optical satellite images is a fundamental and important material for remote sensing applications. The advanced atmospheric corrections have achieved great progress in the removal of atmospheric effects by using complicated physical-based models. However, the process of image-by-image atmospheric correction may cause bias errors for multitemporal images, which produce temporal inconsistencies and discontinuities over the surface reflectance of invariant ground objects. In this study, a surface reflectance correction is proposed for multispectral and multitemporal satellite images. The surface reflectance correction is determined by using pseudoinvariant features instead of an entire image, and the correction is based on a harmonization technique with temporal-consistency and spectral-consistency constraints. With the constraints, the spectral signatures in multispectral images can be maintained, while the surface reflectance biases in multitemporal images can be removed during the image harmonization. In the method, the pseudoinvariant features are determined by using iterative reweighted multitemporal and multivariate alteration detection, called IRMMAD, which is an extension of IRMAD. The multispectral and multitemporal surface reflectance bias removal is formulated as an optimization problem, and a least-squares linear system is solved for optimal harmonization. Qualitative and quantitative analyses on six atmospheric corrections (AC) models multitemporal images have been conducted, and the methods are evaluated using the measurements of spectral and temporal consistencies. The experimental results show that the surface reflectance biases can be significantly removed while the spectral signatures can be preserved. In addition, the proposed method outperforms related harmonization methods in terms of consistency measurements.

1. INTRODUCTION

In Landsat satellite generations, the most popular coverage products are Landsat generations, especially Landsat 5 TM, Landsat 7 ETM+, and Landsat 8 OLI, which spans almost three decades orbiting. They provide radiometric products at level 1 and level 2. The level 1 and level 2 products convert DN to top-of-atmosphere (TOA) and bottom-of-atmospheric (BOA), respectively. Level 1 product is stored in DN, where the conversion to at-sensor reflectance is provided in the metadata as standard manufacture of the sensor calibration parameters, solar zenith angle, and solar irradiance are registered. Atmospheric correction is a conversion from TOA to BOA. First of all, the data recorded in most remote sensing satellites, especially Landsat generations, are stored in the form of a digital number (DN). Landsat 7 ETM+ and lower generation store DN in 8-bit radiometric resolution. Landsat 8 OLI stores DN in 16-bit radiometric resolution (Reuter et al. 2014). This different resolution is by design produced from the manufacturer (H. K. Zhang, Roy, and Kovalskyy 2016; L. garda Denaro et al. 2018; Franke, Heinzl, and Menz 2006). The sensors' changes can be ignored since the TOA or BOA reflectances are applied using three steps: radiometric conversion, apparent reflectance conversion, and atmospheric (Caselles and Lóópez Garc ́ A 1989; Pu, Landry, and Zhang 2015; Helder et al. 2013; Nazeer, Nichol, and Yung 2014; E. F. Vermote and Kotchenova 2008; Teillet and Fedosejevs 1995; Xu 2006). Radiometric conversion and apparent reflectance conversion, conversion from DN to TOA product, are undoubtedly implemented, associating the sensor calibration coefficients, solar zenith angle, and solar irradiance at the top of the atmosphere (H. Zhang, Zimba, and Nzewi 2019; L. G. Denaro and Lin 2020; El Hajj et al. 2008; Paolini et al. 2006; Helder et al. 2013). However, from TOA to the BOA product, the atmospheric correction is more complicated to implement depending on atmospheric data availability (Pu, Landry, and Zhang 2015; Helder et al. 2013; Nazeer, Nichol, and Yung 2014; E. F. Vermote and Kotchenova 2008; Teillet and Fedosejevs 1995; Xu 2006). It needs to quantitatively measure the multiple scattering and absorption due to air molecule and gaseous components, especially for aerosols in the visible region of the electromagnetic spectrum (Pinto, Jing, and Leigh 2020; Pu, Landry, and Zhang 2015). Some of the atmospheric corrections have been proposed. Those using radiative transfer algorithm and atmospheric characterization data quantitatively account for the best result to automatically correct large optical images (E. Vermote et al. 2016; Caselles and Lóópez Garc ́ A 1989). However, the evaluation on the methodology is evaluated by some researchers that the BOA product still less accurate or unreliable, especially in visible spectrum due to aerosol optical thickness (AOT) (Claverie et al. 2015; 2018). Those using radiometric and atmospheric corrections successfully reduce the difference among images with their different basic concept. Radiometric correction is performed in TOA reflectance, in which the atmospheric effect remains to obscure the true object properties. In other words, a radiometric correction method is applied to TOA to minimize the numeric differences among images to a common radiometric level. However, the common radiometric

level is a relative level that cannot represent the true surface object properties. In contrast, atmospheric correction is performed to generate BOA reflectance, representing the absence of atmospheric scattering or absorption. Thus, BOA adopts the absolute method that the converted values can represent the physical object properties (Hu et al. 2011). However, atmospheric correction is limited by some factors and remains minor-existed atmospheric variation when applied to multitemporal images. It is due to many factors, such as the directional effect caused by various view angles from the nadir, estimation of Earth's surface by Lambertian model, and complicated atmospheric quantification modeling (Skakun et al. 2017; Hansen et al. 2014; E. Vermote et al. 2016).

The motivation is to transform its remaining atmospheric variations between multitemporal images under the common reflectance level. The need to convert into a common reflectance level is a fundamental preprocessing procedure before further application analysis. Generally, in most relative correction methods, the transformation needs to select a reference image as a standard common radiometric level. The reference image selected is the clearest overall image. However, the clearest image definition is still discussed, and it is hard to define how clearest the reference image. The idea to transform all images into reference levels is, in other words, not a global optimal. It may lead to propagation error in which other images fall far from the reference. (Pan et al. 2010; Chen et al. 2014) considered the middle image with the minimum distance to the other target images as the reference image, which did not consider image quality. (Cresson and Saint-Geours 2015) adds the constraint of both the sum of the mean values and the sum of the standard deviations. These play an essential role in similar overall images without a reference image. However, their harmonization may lead to inconsistency between spectral bands.

2. Methodology

2.1. Iterative reweighted multitemporal alteration detection

Generalized canonical correlation analysis (GCCA) is the extension of CCA, detecting PIFs from multitemporal images simultaneously. GCCA-based MAD can be called as original GCCA method or multitemporal MAD (MMAD). In the literature, several methods exist to find amount components such as maximization of a function of correlations, maximization of covariances' function, and the combination of correlations and covariances. The maximization of a function of correlations, consists of three criteria, namely summation of correlation method (SUMCOR), the summation of squared correlation method (SSQCOR), and summation of absolute values of the correlation method (SABSCOR). In this study, SUMCOR is the main part of defining PIFs to find their maximum correlation. Consider that a block of random vectors \mathbf{X} is defined in the previous subchapter 2.2.2 that have the dimensional matrix $\in \mathbb{R}^{s \times n}$, where s is the spectral band number $i = 1, \dots, s$ and n is the intensities $i = 1, \dots, n$. The corresponding non-random vectors $\mathbf{A} = [\mathbf{a}_1, \dots, \mathbf{a}_s]^T$ is the eigenvectors with the dimension $\in \mathbb{R}^{s \times s}$ derived from \mathbf{X} . In the multitemporal images, the definition of variable \mathbf{X} can be identified as \mathbf{X}_j and \mathbf{X}_k where $j, k = 1, \dots, m$ with the condition $j \neq k$. In an implementation, SSQCOR is equal to square and SABSCOR is equal to absolute which can be used to find the closeness of the model, and SUMCOR is equal to identity that can be used for finding maximization of positively correlated components denoted as:

$$\underset{\mathbf{a}_1, \dots, \mathbf{a}_m}{\text{maximize}} C_{jk} \sum_{j,k=1:j \neq k}^m g \left(\rho(\mathbf{a}_j^T \mathbf{X}_j, \mathbf{a}_k^T \mathbf{X}_k) \right), \quad (1)$$

subject to the constraints $Var\{\mathbf{a}_j^T \mathbf{X}_j\} = 1, g = (1)$.

In equation 1, the scheme of networking multitemporal image dates is defined by the variable $C_{jk} = 1$ if \mathbf{X}_j and \mathbf{X}_k are connected and $C_{jk} = 0$ if not connected. Reformulated Equation 1 as:

$$\underset{\mathbf{a}_1, \dots, \mathbf{a}_m}{\text{maximize}} \sum_{j,k=1:j \neq k}^m C_{jk} \mathbf{a}_j^T \boldsymbol{\Sigma}_{jk} \mathbf{a}_k = \frac{\mathbf{a}_j^T \boldsymbol{\Sigma}_{jk} \mathbf{a}_k}{\sqrt{\mathbf{a}_j^T \boldsymbol{\Sigma}_{jj} \mathbf{a}_j \mathbf{a}_k^T \boldsymbol{\Sigma}_{kk} \mathbf{a}_k}}, \quad (2)$$

subject to the constraints $\mathbf{a}_j^T \boldsymbol{\Sigma}_{jj} \mathbf{a}_j = \mathbf{a}_k^T \boldsymbol{\Sigma}_{kk} \mathbf{a}_k = 1, j, k = 1, \dots, m,$

where $\boldsymbol{\Sigma}_{jj} = E(\mathbf{X}_j \mathbf{X}_j^T), \boldsymbol{\Sigma}_{kk} = E(\mathbf{X}_k \mathbf{X}_k^T),$ and $\boldsymbol{\Sigma}_{jk} = E(\mathbf{X}_j \mathbf{X}_k^T)$. After defining the algorithm of maximization of correlation, the aid of Lagrangian function is needed to optimize the correlation as described below:

$$F(\mathbf{a}_1, \dots, \mathbf{a}_m, \lambda_1, \dots, \lambda_m) = \sum_{j,k=1; j \neq k}^m C_{jk} \mathbf{a}_j^T \Sigma_{jk} \mathbf{a}_k - \sum_{j=1}^m \frac{\lambda_j}{2} (\mathbf{a}_j^T \Sigma_{jj} \mathbf{a}_j - \mathbf{1}), \quad (3)$$

where $\lambda_1, \dots, \lambda_m$ are the Lagrange multiplier corresponding to $\mathbf{a}_1, \dots, \mathbf{a}_m$ of the linear combination of non-random values or outer weight vectors. Therefore, the canceling derivative concerning λ_m and \mathbf{a}_m of the Lagrange yields the following stationary equations:

$$\Sigma_{jj}^{-1} \sum_{j,k=1; j \neq k}^m C_{jk} (\mathbf{a}_j^T \Sigma_{jk} \mathbf{a}_k) \Sigma_{jk} \mathbf{a}_k = \lambda_j \mathbf{a}_j \quad ; j = 1, \dots, m \quad (4)$$

The stationary Equation stated in Eq. (4) has no analytical solution. The other way to optimize the problem (1) is to build a monotonically convergent algorithm. The primary purpose of building monotonically convergent is to determine the Eigenvectors corresponding to their linear combination. In addition to building monotonically convergent, the PLS algorithm introduced by Wold in 1985 is done to substitute the inner component. The inner component V_j is useful to simplify the equation for GCCA expressed as:

$$V_j = \sum_{k=1; k \neq j}^J C_{jk} \mathbf{a}_k^T \mathbf{X}_k, \quad (5)$$

Therefore, by the use of inner component V_j , the stationary Equation in (4) can be simplified using the following expression:

$$\begin{aligned} Cov(\mathbf{X}_j, V_j) &= E \left(\mathbf{X}_j \sum_{k=1; k \neq j}^m C_{jk} \mathbf{a}_k^T \mathbf{X}_k \right), \\ Cov(\mathbf{X}_j, V_j) &= \sum_{k=1; k \neq j}^m C_{jk} \Sigma_{jk} \mathbf{a}_k. \end{aligned} \quad (6)$$

Further, the outer weight vectors \mathbf{a}_j can be generated by substituting of inner component (5) respected to their constraints (1), then the stationary Equation becomes (4) stated as follows:

$$\begin{aligned} \mathbf{a}_j &= \frac{1}{\lambda_j} \Sigma_{jj}^{-1} \sum_{k=1; k \neq j}^n C_{jk} (\mathbf{a}_j^T \Sigma_{jk} \mathbf{a}_k) \Sigma_{jk} \mathbf{a}_k \\ &= \frac{1}{\lambda_j} \Sigma_{jj}^{-1} Cov(\mathbf{X}_j, V_j) \end{aligned} \quad (7)$$

$$\mathbf{a}_j = [Cov(\mathbf{X}_j, V_j)^T \Sigma_{jj}^{-1} Cov(\mathbf{X}_j, V_j)]^{-\frac{1}{2}} \Sigma_{jj}^{-1} Cov(\mathbf{X}_j, V_j) \quad ; j = 1, \dots, m.$$

Therefore, the equation above can be reconstructed for multitemporal purpose simultaneously described as:

$$f(\mathbf{a}_1, \mathbf{a}_2, \dots, \mathbf{a}_m) = \sum_{j,k=1; k \neq j}^m C_{jk} \rho(\mathbf{a}_j^T \mathbf{X}_j, \mathbf{a}_k^T \mathbf{X}_k) \quad (8)$$

The termination criterion, \mathbf{a}_j will converge at a certain point using the Gauss-Seidel algorithm for solving a system of linear equations and several other iterative algorithms such as the Wold and Hanafi's PLS algorithm, supposing that $f(\mathbf{a}_1, \mathbf{a}_2, \dots, \mathbf{a}_m) \leq f(\mathbf{a}_1^{t+1}, \mathbf{a}_2^{t+1}, \dots, \mathbf{a}_m^{t+1})$ where t is iteratively replacing the previous value.

2.2. Constrained Harmonization

This method is also called as the referenceless method harmonization. Assume that the robust PIFs are already extracted. The following statistical parameters, such as mean and standard deviation, are used for the extracted PIFs. The key in globally optimized normalization is to optimize the mean and standard deviation difference close to zero using linear least-square optimization. The linear parameters of variation between images, before and after processing, can be described in $x'_j = x_j \times \alpha_j + \beta_j$. Thus, the value of the mean of the image before and after normalization is described as:

$$\bar{x}'_j = \frac{1}{n} \sum_{i=1}^n x'_{ij} = \alpha_j \times \frac{1}{n} \sum_{i=1}^n x_{ij} + \beta_j = \alpha_j \bar{x}_j + \beta_j, \quad j = 1, \dots, J. \quad (9)$$

Similarly, the value of the standard deviation before and after normalization is described as:

$$\begin{aligned} \sigma_{x'_j} &= \sqrt{\frac{1}{n} \sum_{i=1}^n (x'_{ij} - \bar{x}'_j)^2} \\ &= \sqrt{\frac{1}{n} \sum_{i=1}^n ((\alpha_j x_{ij} + \beta_j) - (\alpha_j \bar{x}_j + \beta_j))^2} = \alpha_j \sigma_{x_j}, \end{aligned} \quad (10)$$

where \bar{x}_j , \bar{x}'_j and σ_{x_j} , $\sigma_{x'_j}$ are the means and standard deviation values before and after normalization, respectively. Consider that the images j and k are at the same location and captured at different times. Therefore, the mean and standard deviation are expressed as \bar{x}_j , σ_j , \bar{x}_k , and σ_k . Similarly, to the coefficients of images j and k are α_j , β_j and α_k , β_k , respectively. The difference of mean and standard deviation after normalization should have corresponded to the equal value as the Equation below:

$$\begin{aligned} \bar{x}'_j - \bar{x}'_k &= 0, \\ \sigma'_j - \sigma'_k &= 0, \end{aligned} \quad (11)$$

However, Eq. 11 is not working in the ideal condition. The images taken under different dates remain biased. Thus, a little difference still exists, and the Equation is reformulated as:

$$\begin{aligned} \Delta \bar{x}_{jk} &= \bar{x}'_j - \bar{x}'_k, \\ \Delta \sigma_{jk} &= \sigma'_j - \sigma'_k, \end{aligned} \quad (12)$$

where $\Delta \bar{x}_{jk}$, $\Delta \sigma_{jk}$ are the difference between the mean and standard deviation exist at the time j and k after normalization, respectively. Then, the normalization condition can be reformulated as:

$$\begin{aligned} \Delta \bar{x}_{jk} &= \bar{x}'_j - \bar{x}'_k = \alpha_j \bar{x}_j + \beta_j - (\alpha_k \bar{x}_k + \beta_k), \\ \Delta \sigma_{jk} &= \sigma'_j - \sigma'_k = \alpha_j \sigma_j - \alpha_k \sigma_k. \end{aligned} \quad (13)$$

According to the least-square optimization, the optimal condition for finding the minimal error is stated as

$$\begin{aligned} \mathbf{W} \mathbf{A} \mathbf{v} &= \mathbf{b}, \text{ where,} \\ \mathbf{b} &= [\Delta \bar{x}_{jk} \quad \Delta \sigma_{jk}]^T, \\ \mathbf{v} &= [\alpha_j \quad \beta_j \quad \alpha_k \quad \beta_k]^T, \\ \mathbf{W} &= \begin{bmatrix} w_j & 0 \\ 0 & w_k \end{bmatrix}. \end{aligned} \quad (14)$$

For the matrix \mathbf{A} ,

$$\mathbf{A} = \begin{bmatrix} \bar{x}_j & 1 & -\bar{x}_k & -1 \\ \sigma_j & 0 & -\sigma_k & 0 \end{bmatrix}. \quad (15)$$

Since the number of the Equation is two for bitemporal images, and the unknown parameters are four, that is, $\alpha_j, \beta_j, \alpha_k$, and β_k . Therefore, the constraints are required to generate four equations for the four outputs parameters of bitemporal images. The constraint \mathbf{c} is regenerated for the least-square $\mathbf{WAv} = \mathbf{b} - \mathbf{c}$ in which the Equation becomes:

$$\mathbf{c} = [0 \quad 0 \quad \alpha_k \quad \beta_k]^T, \quad (16)$$

hence the least-square becomes:

$$\mathbf{WAv} + \mathbf{c} = \mathbf{b}. \quad (17)$$

From the temporal-constraints:

$$\begin{aligned} \Delta \bar{x}_{kk} &= \bar{x}'_k - \bar{x}_k = \alpha_k \bar{x}_k + \beta_k - \bar{x}_k, \\ \Delta \sigma_{kk} &= \sigma'_k - \sigma_k = \alpha_k \sigma_k - \sigma_k. \end{aligned} \quad (18)$$

The temporal-constraint employed in this Equation are to close the values before and after normalization. Then, \mathbf{b} is updated as:

$$\mathbf{b} = [\Delta \bar{x}_{jk} \quad \Delta \sigma_{jk} \quad \Delta \bar{x}_{kk} \quad \Delta \sigma_{kk}]^T. \quad (19)$$

Corresponds to the matrix \mathbf{A} is updated as:

$$\mathbf{A} = \begin{bmatrix} \bar{x}_j & 1 & -\bar{x}_k & -1 \\ \sigma_j & 0 & -\sigma_k & 0 \\ 0 & 0 & \bar{x}_k & 1 \\ 0 & 0 & \sigma_k & 0 \end{bmatrix}. \quad (20)$$




Thus, after solving the Equation $\mathbf{v} = (\mathbf{A}^T \mathbf{W} \mathbf{A})^{-1} \mathbf{A}^T \mathbf{W} (\mathbf{b} + \mathbf{c})$, the coefficients are retrieved at the minimum error. The equations above are applied to the bitemporal images j and k . However, it also can be used for multitemporal images l, m, n , etc.

3. RESULTS AND DISCUSSIONS

3.1. Datasets

Three study areas that contain various landscapes, including an agricultural and lake, urban, forest as shown in Table 1, were selected for method evaluation. Thus, three datasets in each location are tested in purpose with multitemporal images simultaneously. In dataset I, each of the year data from 2013 to 2016 are acquired under a similar season. The heterogeneous data, including forest, urban, agricultural, are chosen in the study, similar to dataset III with the higher image resolution. In the dataset II and IV, the water bodies are included in a scene with vegetation in the major coverage, but dataset IV have significant cloud covers than dataset II. Dataset IV is chosen so that the PIFs quality is easily understood with significant changes from multitemporal images.

Table 1. Study areas and tested data

Dataset #			
	I	II	III
Location (path, row)	Indonesia (124, 062)	France (201, 033)	Taiwan (117, 043)
Acquisitions date	2015/06/26	2017/08/13	2013/04/16
	2016/12/05	2018/07/31	2016/06/27
	2017/08/02	2019/05/31	2017/08/17
	2019/09/09	2020/09/06	2018/09/21
Landscapes	Agricultural	Heterogeneous	Vegetation
Image size	2000 x 2000	3000 x 3000	1900 x 1800

3.2. PIFs extraction

In the framework of IRMMAD, the computation of covariance matrix and temporal weighting is easily affected when there are significant land cover changes or cloud existence in multitemporal images. Compared to the original MMAD, the initial weight is set to 1 for all pixels that hardly separate between PIFs and non-PIFs. The IRMMAD uses spectral angle noticed to be suitable for initial weight. The extracted PIFs are used in reflectance harmonization and evaluation. Therefore, a quantitative assessment is necessary to figure out the quality of the extracted PIFs. This quality is calculated by utilizing Pearson's correlation coefficient, which is commonly used to measure the linear correlation between two variables. The range of this coefficient is [-1,1], where 1 represents the strongest positive correlation, -1 denotes the strongest negative correlation, and 0 indicates no correlation.

Table 2. PIFs quality of each multitemporal image datasets

Band #	PIFs Quality		
	Dataset I	Dataset II	Dataset III
1	0.89691	0.92957	0.77121
2	0.90503	0.94263	0.77241
3	0.91943	0.93674	0.80709
4	0.87373	0.95020	0.82367
5	0.88526	0.83781	0.87946
6	0.91533	0.95932	0.89135
7	0.90860	0.94210	0.88978

3.3. Image harmonization

In case that acceptable PIFs are extracted, the following step is a key to conduct reflectance harmonization. In the previous studies, the most common normalization method is using band-by-band harmonization normalization. It means that the generation of coefficient determinations is applied to each band to find optimal minimum errors independently. The coefficient determinations are certainly affecting inconsistency of spectral signature of before and after normalization. The number of coefficient transformations such as slope and intercept can be constrained by such a factor that the spectral signature is preserved. The weighting function is applied to the reflectance harmonization, and then the two weighting factors are conducted in both band-by-band constrained and gradient constrained. For visual comparison, the multitemporal images are tested and mosaicked by the side horizontally, as seen in the discontinuity line or brightness shown in Figures 1 - 3. The multitemporal images used can set more than three images or even limitless sequentially from different dates and years to harmonize the spectral inconsistency simultaneously. However, for the evaluation purpose, three images are enough to test the feasibility of the proposed method. As seen in Figures 1 - 3, the discontinuity is apparent for the original image mosaicking. Thus, the improvement exists after the normalization procedure is conducted, the discontinuity line reduces to smooth or disappear. However, it is hard to distinguish the difference between constrained harmonization with various weighting sets visually.

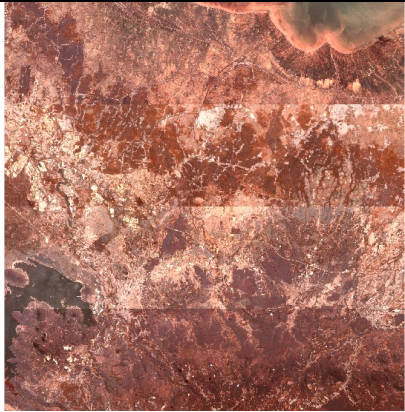
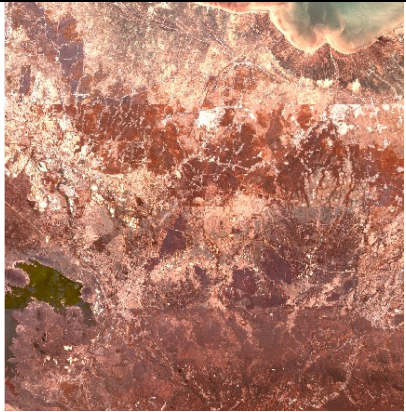
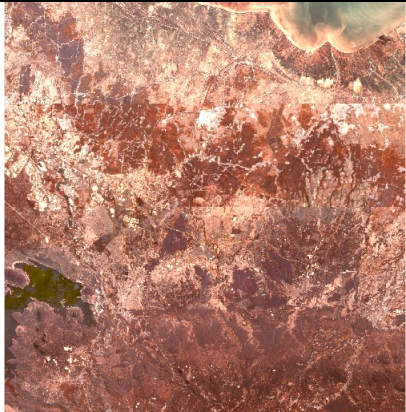
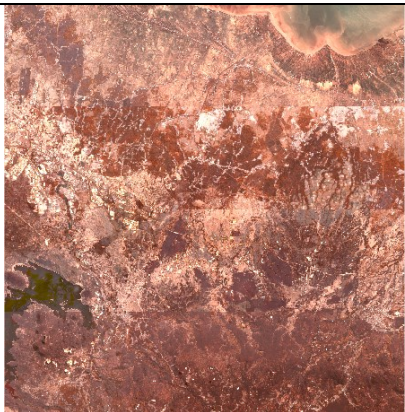
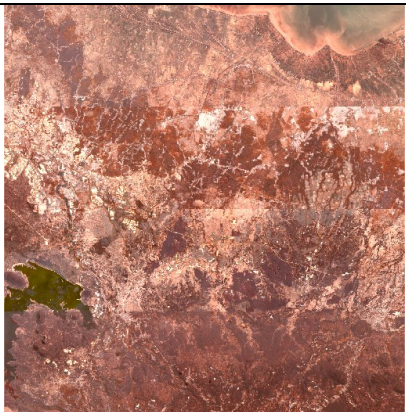
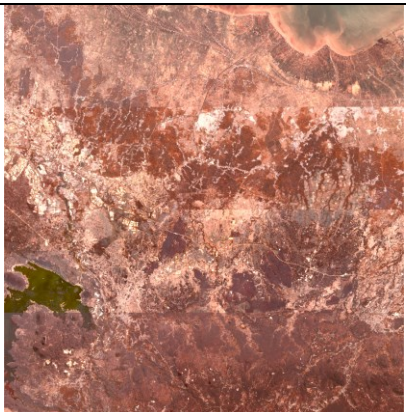
Dataset I		
Original Image	Temporal harmonization	
	$\omega = 0.1$	$\omega = 1$
		
Temporal and spectral harmonization		
$\omega = 0.1$	$\omega = 0.3$	$\omega = 0.7$
		

Figure 1. Result of Dataset II. Top: 1st column is original tested images (mosaicked to be a composed image); 2nd and 3rd columns are band-by-band harmonization result with ω is equal to 0.1 and 1 respectively. Bottom: 1st, 2nd, 3rd are constrained harmonization results of the proposed method with ω is continuously set to 0.1, 0.3, and 0.7, respectively.

Dataset II		
Original Image	Temporal harmonization	
	$\omega = 0.1$	$\omega = 1$

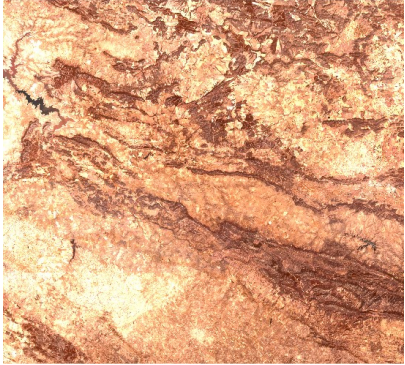
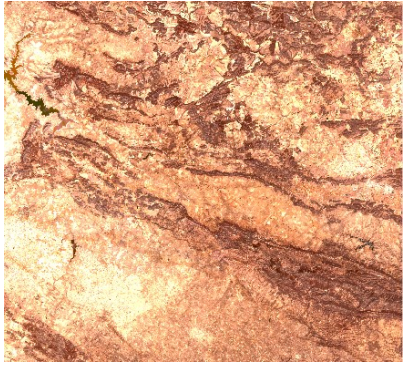
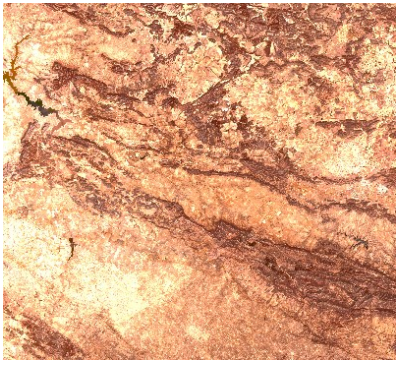
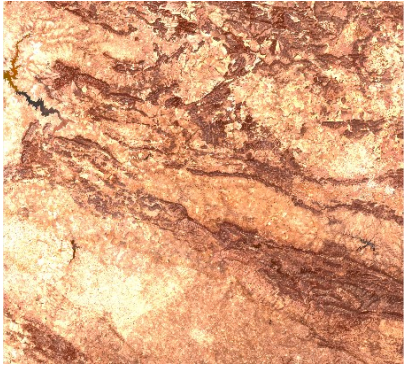
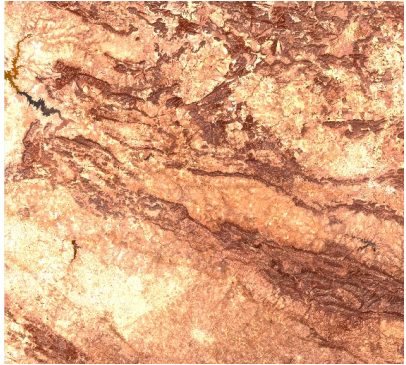
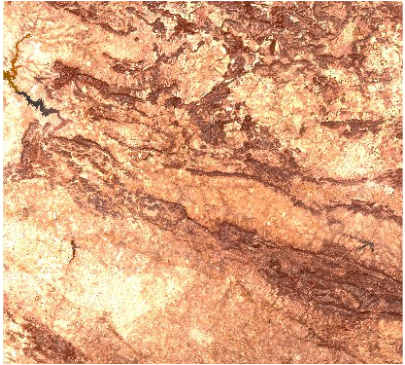



		
Temporal and spectral harmonization		
$\omega = 0.1$	$\omega = 0.3$	$\omega = 0.7$
		

Figure 2. Result of Dataset III. Top: 1st column is original tested images (mosaicked to be a composed image); 2nd and 3rd columns are band-by-band harmonization result with ω is equal to 0.1 and 1 respectively. Bottom: 1st, 2nd, 3rd are constrained harmonization results of the proposed method with ω is continuously set to 0.1, 0.3, and 0.7, respectively.

Dataset III		
Original Image	Temporal harmonization	
	$\omega = 0.1$	$\omega = 1$
		

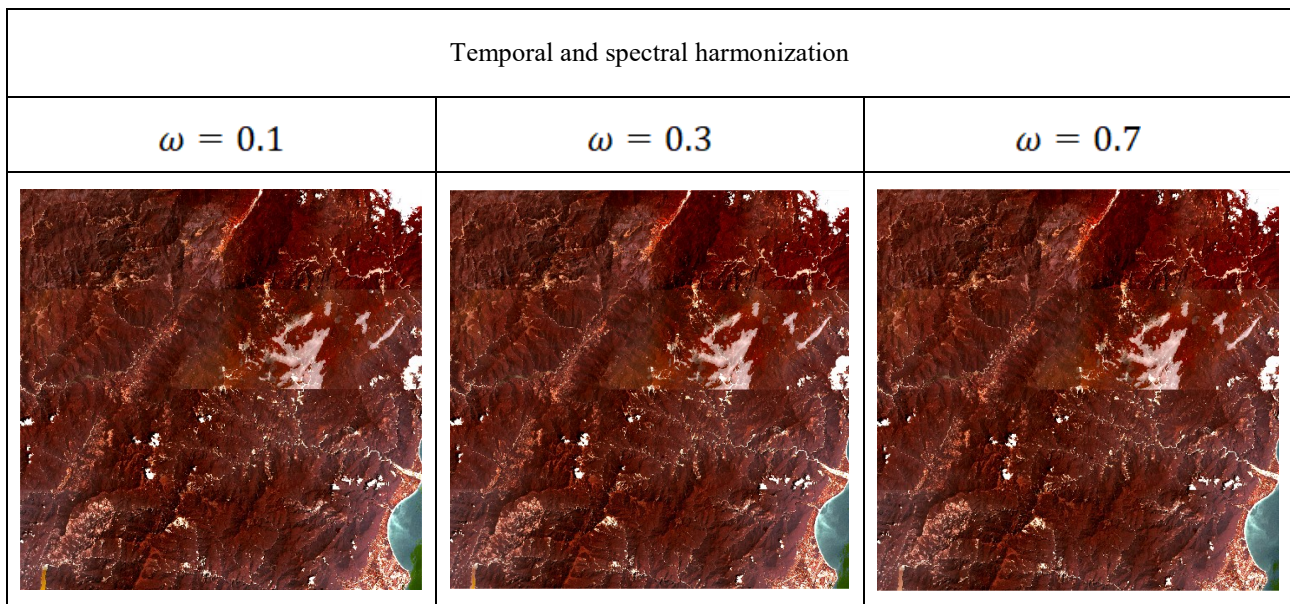


Figure 3. Result of Dataset IV. Top: 1st column is original tested images (mosaicked to be a composed image); 2nd and 3rd columns are band-by-band harmonization result with ω is equal to 0.1 and 1 respectively. Bottom: 1st, 2nd, 3rd are constrained harmonization results of the proposed method with ω is continuously set to 0.1, 0.3, and 0.7, respectively.

4. CONCLUSION

The study presents the constrained harmonization normalization method, generating better spectral consistency and harmonization quality than the related method. The main part of the proposed method is addressed on the PIFs extraction and the harmonization. In terms of PIFs extraction, iterative reweighted multitemporal multivariate alteration detection (IRMGCCA) is the best method considering spectral weighting and temporal weighting iteratively to extract PIFs. Once the PIFs are extracted using IRMGCCA, a normalization to obtain coefficient transformation is required to process harmonization. The disadvantage of the temporal harmonization is that spectral inconsistency may happen due to preservation in temporal-domain only. The novel constrained harmonization is proposed to perform normalization with optimal results in which both temporal consistency and spectral consistency are satisfied. In the experiment, the comparison of three on-demand level-2 Landsat 8 OLI images were tested and show that the proposed method results the consistency in the spectral signature.

5. REFERENCES

- Caselles, V., and M. J. López Garc Í A. 1989. "An Alternative Simple Approach to Estimate Atmospheric Correction in Multitemporal Studies." *International Journal of Remote Sensing* 10 (6): 1127–34. <https://doi.org/10.1080/01431168908903951>.
- Chen, Chong, Zhenjie Chen, Manchun Li, Yongxue Liu, Liang Cheng, and Yibin Ren. 2014. "Parallel Relative Radiometric Normalisation for Remote Sensing Image Mosaics." *Computers and Geosciences* 73: 28–36. <https://doi.org/10.1016/j.cageo.2014.08.007>.
- Claverie, Martin, Junchang Ju, Jeffrey G. Masek, Jennifer L. Dungan, Eric F. Vermote, Jean Claude Roger, Sergii V. Skakun, and Christopher Justice. 2018. "The Harmonized Landsat and Sentinel-2 Surface Reflectance Data Set." *Remote Sensing of Environment* 219 (October): 145–61. <https://doi.org/10.1016/j.rse.2018.09.002>.
- Claverie, Martin, Eric F. Vermote, Belen Franch, and Jeffrey G. Masek. 2015. "Evaluation of the Landsat-5 TM and Landsat-7 ETM+ Surface Reflectance Products." *Remote Sensing of Environment* 169: 390–403. <https://doi.org/10.1016/j.rse.2015.08.030>.
- Cresson, Remi, and Nathalie Saint-Geours. 2015. "Natural Color Satellite Image Mosaicking Using Quadratic Programming in Decorrelated Color Space." *IEEE Journal of Selected Topics in Applied Earth Observations and Remote Sensing* 8 (8): 4151–62. <https://doi.org/10.1109/JSTARS.2015.2449233>.
- Denaro, Lino garda, Bo-Yi Lin, Muhammad Aldila Syariz, and Chao-Hung Lin. 2018. "Pseudoinvariant Feature Selection for Cross-Sensor Optical Satellite Images." *Journal of Applied Remote Sensing* 11 (1). <https://doi.org/10.1117/1.JRS>.
- Denaro, Lino Garda, and Chao Hung Lin. 2020. "Hybrid Canonical Correlation Analysis and Regression for Radiometric Normalization of Cross-Sensor Satellite Imagery." *IEEE Journal of Selected Topics in Applied*



- Earth Observations and Remote Sensing* 13: 976–86. <https://doi.org/10.1109/JSTARS.2020.2971857>.
- Franke, J., V. Heinzl, and G. Menz. 2006. "Assessment of NDVI- Differences Caused by Sensor-Specific Relative Spectral Response Functions." *International Geoscience and Remote Sensing Symposium (IGARSS)*, 1138–41. <https://doi.org/10.1109/IGARSS.2006.294>.
- Hajj, Mahmoud El, Agnès Bégué, Bruno Lafrance, Olivier Hagolle, Gérard Dedieu, and Matthieu Rumeau. 2008. "Relative Radiometric Normalization and Atmospheric Correction of a SPOT 5 Time Series." *Sensors* 8 (4): 2774–91. <https://doi.org/10.3390/s8042774>.
- Hansen, M. C., A. Egorov, P. V. Potapov, S. V. Stehman, A. Tyukavina, S. A. Turubanova, D. P. Roy, et al. 2014. "Monitoring Conterminous United States (CONUS) Land Cover Change with Web-Enabled Landsat Data (WELD)." *Remote Sensing of Environment* 140: 466–84. <https://doi.org/10.1016/j.rse.2013.08.014>.
- Helder, Dennis, Kurtis J. Thome, Nischal Mishra, Gyanesh Chander, Xiaoxiong Xiong, Amit Angal, and Taeyoung Choi. 2013. "Absolute Radiometric Calibration of Landsat Using a Pseudo Invariant Calibration Site." *IEEE Transactions on Geoscience and Remote Sensing* 51 (3): 1360–69. <https://doi.org/10.1109/TGRS.2013.2243738>.
- Hu, Yong, Liangyun Liu, Lingling Liu, and Qunjun Jiao. 2011. "Comparison of Absolute and Relative Radiometric Normalization Use Landsat Time Series Images." *MIPPR 2011: Remote Sensing Image Processing, Geographic Information Systems, and Other Applications* 8006 (November 2011): 800616. <https://doi.org/10.1117/12.902076>.
- Nazeer, Majid, Janet E. Nichol, and Ying Kit Yung. 2014. "Evaluation of Atmospheric Correction Models and Landsat Surface Reflectance Product in an Urban Coastal Environment." *International Journal of Remote Sensing* 35 (16): 6271–91. <https://doi.org/10.1080/01431161.2014.951742>.
- Pan, Jun, Mi Wang, Deren Li, and Junli Li. 2010. "A Network-Based Radiometric Equalization Approach for Digital Aerial Orthoimages." *IEEE Geoscience and Remote Sensing Letters* 7 (2): 401–5. <https://doi.org/10.1109/LGRS.2009.2037442>.
- Paolini, Leonardo, Francisco Grings, José Sobrino, Juan C. Jiménez Muñoz, and Haydee Karszenbaum. 2006. "Radiometric Correction Effects in Landsat Multi-Date/Multi-Sensor Change Detection Studies." *International Journal of Remote Sensing* 27 (4): 685–704. <https://doi.org/10.1080/01431160500183057>.
- Pinto, Cibele Teixeira, Xin Jing, and Larry Leigh. 2020. "Evaluation Analysis of Landsat Level-1 and Level-2 Data Products Using in Situ Measurements." *Remote Sensing* 12 (16). <https://doi.org/10.3390/RS12162597>.
- Pu, Ruiliang, Shawn Landry, and Jingcheng Zhang. 2015. "Evaluation of Atmospheric Correction Methods in Identifying Urban Tree Species with WorldView-2 Imagery." *IEEE Journal of Selected Topics in Applied Earth Observations and Remote Sensing* 8 (5): 1886–97. <https://doi.org/10.1109/JSTARS.2014.2363441>.
- Reuter, Dennis, Brian Wenny, Matthew Montanaro, Zelalem Tesfaye, and Allen Lunsford. 2014. "Radiometric Calibration Methodology of the Landsat 8 Thermal Infrared Sensor." *Remote Sensing* 6 (9): 8803–21. <https://doi.org/10.3390/rs6098803>.
- Skakun, Sergii, Eric Vermote, Jean-Claude Roger, and Belen Franch. 2017. "Combined Use of Landsat-8 and Sentinel-2A Images for Winter Crop Mapping and Winter Wheat Yield Assessment at Regional Scale." *AIMS Geosciences* 3 (2): 163–86. <https://doi.org/10.3934/geosci.2017.2.163>.
- Teillet, P. M., and C. Fedosejevs. 1995. "On the Dark Target Approach to Atmospheric Correction of Remotely Sensed Data." *Canadian Journal of Remote Sensing* 21 (4): 374–87. <https://doi.org/10.1080/07038992.1995.10855161>.
- Vermote, Eric F., and Svetlana Kotchenova. 2008. "Atmospheric Correction for the Monitoring of Land Surfaces." *Journal of Geophysical Research Atmospheres* 113 (23): 1–12. <https://doi.org/10.1029/2007JD009662>.
- Vermote, Eric, Chris Justice, Martin Claverie, and Belen Franch. 2016. "Preliminary Analysis of the Performance of the Landsat 8/OLI Land Surface Reflectance Product." *Remote Sensing of Environment* 185: 46–56. <https://doi.org/10.1016/j.rse.2016.04.008>.
- Xu, Hanqiu. 2006. "Evaluation of Two Absolute Radiometric Normalization Algorithms for Pre-Processing of Landsat Imagery." *Journal of China University of Geosciences* 17 (2). [https://doi.org/10.1016/S1002-0705\(06\)60020-4](https://doi.org/10.1016/S1002-0705(06)60020-4).
- Zhang, Hankui K., David P. Roy, and Valeriy Kovalskyy. 2016. "Optimal Solar Geometry Definition for Global Long-Term Landsat Time-Series Bidirectional Reflectance Normalization." *IEEE Transactions on Geoscience and Remote Sensing* 54 (3): 1410–18. <https://doi.org/10.1109/TGRS.2015.2480684>.
- Zhang, Hua, Paul V. Zimba, and Emmanuel U. Nzewi. 2019. "A New Pseudoinvariant Near-Infrared Threshold Method for Relative Radiometric Correction of Aerial Imagery." *Remote Sensing* 11 (16): 1–17. <https://doi.org/10.3390/rs11161931>.